Journal of Nanobiotechnology

RESEARCH Open Access

DNA binding effects of LDH nanozyme for aseptic osteolysis mitigation through STING pathway modulation

Zi Fu[1], Meng Zhang[1*], Ying Huang[1], Han Wang[1], Wanting Hao[1], Zeyang Liu[1], Haiyan Guo[1*] and Dalong Ni[1*]

Abstract

Persistent and intense inflammation is recognized as the primary cause of wear-particle-induced aseptic osteolysis, which ultimately resulting in aseptic prosthesis loosening. Reducing inflammation plays a significant role in mitigating osteolysis, and the STING pathway has emerged as a promising therapeutic target for its prevention. Specifically, damaged periprosthetic cells of aseptic osteolysis release double-stranded DNA (dsDNA) into the osteolytic microenvironment, serving as a specific stimulus for the STING pathway. Herein, we found that layered double hydroxide (LDH) nanozyme exhibited a robust DNA-binding capacity primarily mediated by van der Waals interactions, which showed superior performance in inhibiting dsDNA-induced inflammation of aseptic osteolysis. Importantly, such binding capability enabled effective co-loading LDH with STING inhibitor C176, thus facilitating inhibition of the STING pathway. Such synergistic actions contributed to ameliorate the inflammatory milieu and remodel the osteolysis microenvironment successfully to reduce cranial bone damage, which was confirmed on animal model of osteolysis. Collectively, this strategy demonstrated an effective approach by utilizing synergistic effects to establish a positive feedback loop in the treatment of osteolysis, thereby alleviating TiPs-induced periprosthetic osteolysis and preventing postoperative complications.

Keywords Inflammation, cGAS-STING pathway, Nanozyme, Oxidative stress, Osteolysis

Introduction

Total joint arthroplasty (TJA) is one of the most successful orthopedic surgical procedures of the 21st century, offering an effective solution for pain relief, joint function restoration, and improved long-term outcomes for patients [1, 2]. However, aseptic loosening of the prosthesis remains a significant late-stage complication, occurring in 5 to 10% of cases within 15 to 20 years post-surgery [3, 4]. Extensive research indicates that biological factors are the primary cause of aseptic loosening around the prosthesis. Wear particles produced by prosthesis-bone interaction trigger periprosthetic cells to release pro-inflammatory factors and chemokines, which lead to chronic aseptic inflammation and increased local oxidative stress [5, 6]. The persistent inflammatory response

*Correspondence:
Meng Zhang
meng.zhang@sjtu.edu.cn
Haiyan Guo
haiyanguo@sjtu.edu.cn
Dalong Ni
ndl12353@rjh.com.cn
[1]Department of Orthopaedics, Shanghai Key Laboratory for Prevention and Treatment of Bone and Joint Diseases, Shanghai Institute of Traumatology and Orthopaedics, Ruijin Hospital, Shanghai Jiao Tong University School of Medicine, Shanghai 200025, P. R. China

disrupts the dynamic equilibrium of periprosthetic bone, resulting in enhanced osteoclastic activity and subsequent periprosthetic osteolysis [7–9]. Though the pathogenesis of periprosthetic osteolysis remains poorly defined, inflammation-induced imbalances in local bone metabolism are widely recognized as the primary cause. Therefore, controlling inflammation is essential for improving the periprosthetic bone microenvironment to restore balance in the inflammatory milieu [10, 11].

Stimulator of interferon genes (STING) has gathered significant interest as a potential treatment targets for inflammatory conditions [12–14]. Dysregulation of the STING pathway has been shown to promote aberrant innate immune responses [15], and further lead to the intracellular homeostasis disruption [16–18]. Moreover, studies indicated a positive correlation between STING/tank-binding protein 1 (TBK1) and titanium particle (TiPs)-induced inflammatory response in macrophages. Since titanium is widely used in prosthesis implants, targeting STING could be a promising strategy for preventing periprosthetic osteolysis. Given the crucial role of STING in inflammatory disorders, recent studies have developed several STING antagonists for inflammatory alleviation. For example, a small molecule drug C176 was demonstrated to effectively inhibit STING activation [19, 20], thereby alleviating inflammation in conditions such as acute lung injury [21], rheumatoid arthritis [22], and pulmonary fibrosis [23]. Consequently, the C176 as a STING signaling inhibitor may present a promising alternative therapy for addressing aseptic prosthetic loosening.

The presence of pro-inflammatory factors potentially trigger various pathological signal transductions [24, 25]. In light of this, eliminating these factors may be an effective approach for STING pathway remodeling. Specifically, in the context of wear particle-induced inflammation and periprosthetic osteolysis, damaged periprosthetic cells release double-stranded DNA (dsDNA) into the osteolytic microenvironment, serving as a specific stimulus for the STING pathway [26]. Upon recognition of this cell-free DNA (cfDNA) by cyclic GMP-AMP synthase (cGAS), STING recruits kinases such as TBK1 and activates interferon regulatory factor 3 (IRF3), promoting their phosphorylation (p-TBK1 and p-IRF3) [27]. Therefore, dsDNA removement could reduce STING activation and subsequently attenuate the inflammatory response. Specially engineered biomaterials have been designed to eliminate cfDNA, with examples including those capable of adsorbing and sequestering cfDNA to inhibit DNA-induced immune responses in macrophages [28, 29]. Among these biomaterials, layered double hydroxides (LDHs) offer several advantages for drug delivery, including targeted delivery, slow release, improved bioavailability and reduced side effects [30–32]. Moreover, LDHs can efficiently scavenge dsDNA and simultaneously deliver STING antagonists to inhibit the STING pathway, suggesting its great potential for osteolysis therapy.

Besides, extant research indicates a close interdependence between oxidative stress and inflammation [11, 33]. High levels of reactive oxygen species (ROS) and oxidative stress products in inflammatory environments amplify pro-inflammatory responses and cellular damage, leading to increased ROS production. Thus, effective scavenging of excess ROS to assuage oxidative stress is considered as a necessary step for alleviating inflammation [34, 35]. LDHs with superoxide dismutase (SODase) activity are capable of stably scavenging ROS due to their excellent antioxidant activity, which can also be loaded with anti-inflammatory drugs to further reduce inflammation. Such dual functionality is consistently effective in various anti-inflammatory treatments, making LDHs a promising candidate to be employed in osteolysis therapy.

In this study, a SODase-like CoAl-LDH (abbreviated as "LDH") was developed to capture cfDNA and locally loaded with C176 (abbreviated as "LDH/C") for periprosthetic osteolysis treatment (Scheme 1). The LDH/C intervenes in cfDNA-associated pro-inflammatory signaling and synergistically inhibits the STING signaling pathway. Additionally, the SODase-like enzyme activity of the LDH plays an integral role in regulating oxidative stress levels in the local microenvironment. A systematic investigation was conducted to examine the capacity and mechanism of LDH/C binding to cfDNA and its impact on the regulation of inflammation in a mouse model of TiPs-induced aseptic osteolysis. The LDH/C was found to mitigate the inflammatory response by inhibiting the cGAS-STING pathway and the subsequent NF-κB signaling cascade. Additionally, SODase-like enzyme activity of LDH/C effectively reduces the intracellular accumulation of ROS and further regulate the inflammatory response by reshaping the oxidative stress environment. Consequently, these interactions inhibit the differentiation of macrophage precursors into osteoclasts, thus regulating aberrant bone homeostasis. This approach integrates STING pathway inhibition with the scavenging of ROS and the removal of cfDNA to form a positive self-reinforcing cycle. In this way, the proposed strategy effectively counters the effects of TiPs-induced periprosthetic osteolysis and minimizes the risk of postoperative complications.

Results and discussion

Synthesis and characterization of LDH and LDH/C

The LDH was prepared following a modified protocol of the reported method (Fig. 1a). Transmission electron microscopy (TEM) images revealed that the synthesised

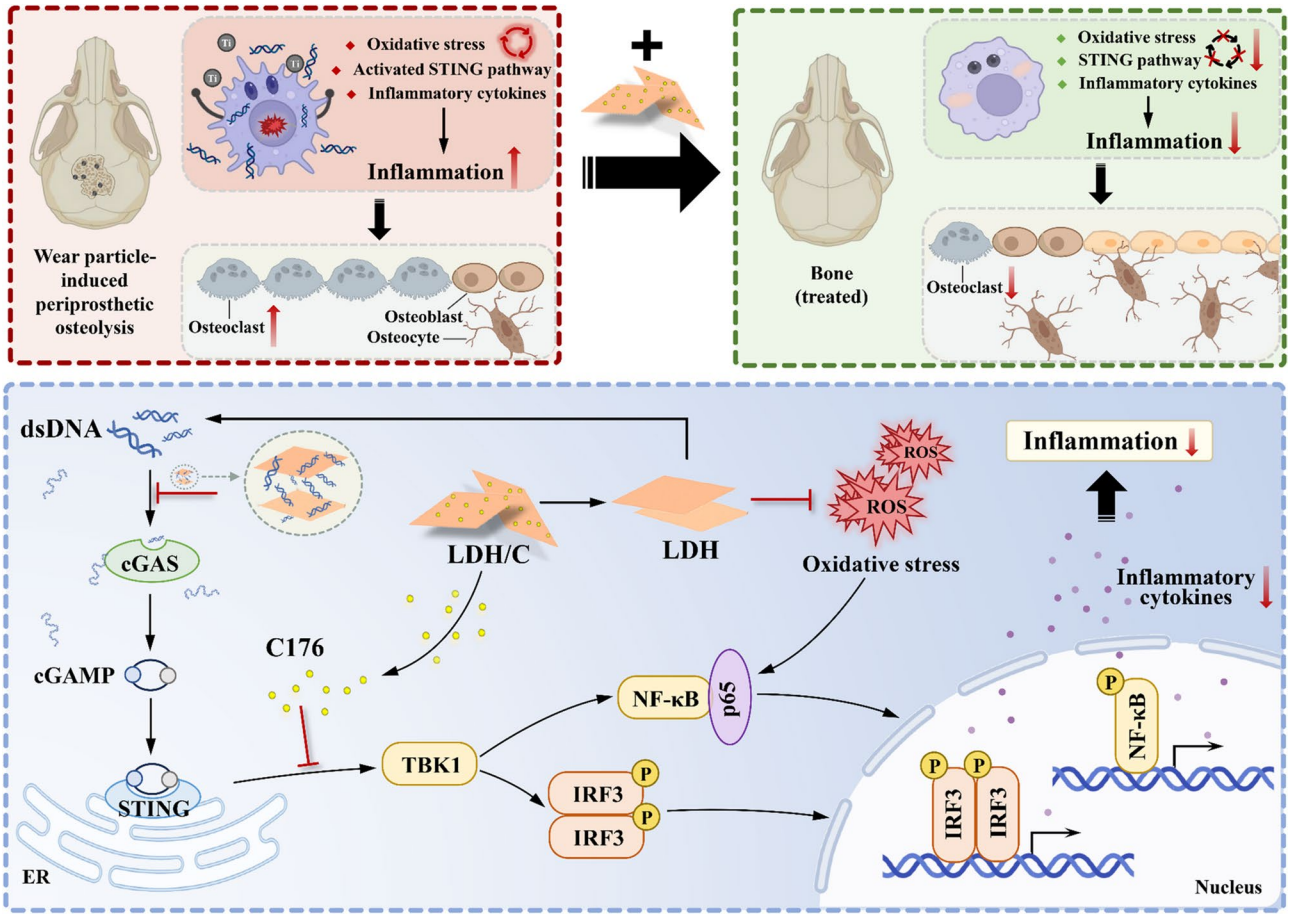

Scheme 1 The synergistic mechanism for the mitigation of aseptic osteolysis with LDH/C-based therapeutics

LDH exhibited a nanosheet morphology with the mean diameter of 51 nm (Fig. 1b, S1). Energy-dispersive X-ray spectroscopy (EDS) analysis revealed the presence of Co, Al, and O in the prepared nanosheet. The nanostructure of the nanosheets was further confirmed using atomic force microscope (AFM), revealing a thickness of approximately 1.39 nm (Fig. 1c-d). However, this value is significantly larger than the theoretical thickness value of a monolayer LDH, which can be attributed to the presence of charge-balancing anions and formamide [36]. The pattern obtained from X-Ray diffractometer (XRD) showed a higher angle (39.6°) shift of the (015) diffraction peak, suggesting the lattice stretching in the (015) plane and the possible introduction of defects in the prepared LDH (Fig. 1e). The speculation was further confirmed by electron spin resonance (ESR) spectroscopy, as the signal at g = 2.003 was detected, demonstrating the presence of oxygen vacancies in LDH (Fig. 1f) [37]. In addition, the prepared LDH was further investigated by X-ray photoelectron sSpectroscopy (XPS) to show the chemical states of the metals surrounding the surface vacancy sites (Fig. 1g, S2). The peaks of Co $2p_{3/2}$ and $2p_{1/2}$ were identified at 780.68 eV and 796.68 eV, respectively. The peak of $2p_{3/2}$ exhibited a proximity to the reported peak position (780.81 eV) in the relevant literature [38], indicating the coexsistence of Co^{2+} and Co^{3+}, which suggested a comparable chemical nature for both species. The ratio of Co^{3+}/Co^{2+} was calculated to be 1.23, which represented the active component of Co-based nanozymes [39], endowing LDH with superior SODase-like activity.

Defect engineering is a promising approach for enhancing the catalytic performance of nanozymes with oxygen vacancies recognized as an effective strategy, which has been already applied for regulating nanozymes [40, 41]. The SODase-like enzyme activity was evaluated using a pyrogallol self-oxidation method, with UV-Vis absorbance measured at a wavelength of 325 nm [42]. The synthesized LDH exhibited SODase-like activity with concentration-dependent behaviors (Fig. 1h), as evidenced by the typical substrate interaction observed in the natural enzyme under physiological circumstances. The clearance performance demonstrated a positive trend with increasing dosage, with 82% scavenging activity at concentrations reached to 100 μg/mL, which is comparable to the efficiencies of reported SODase-mimicking nanozymes in the literature [43–45]. The

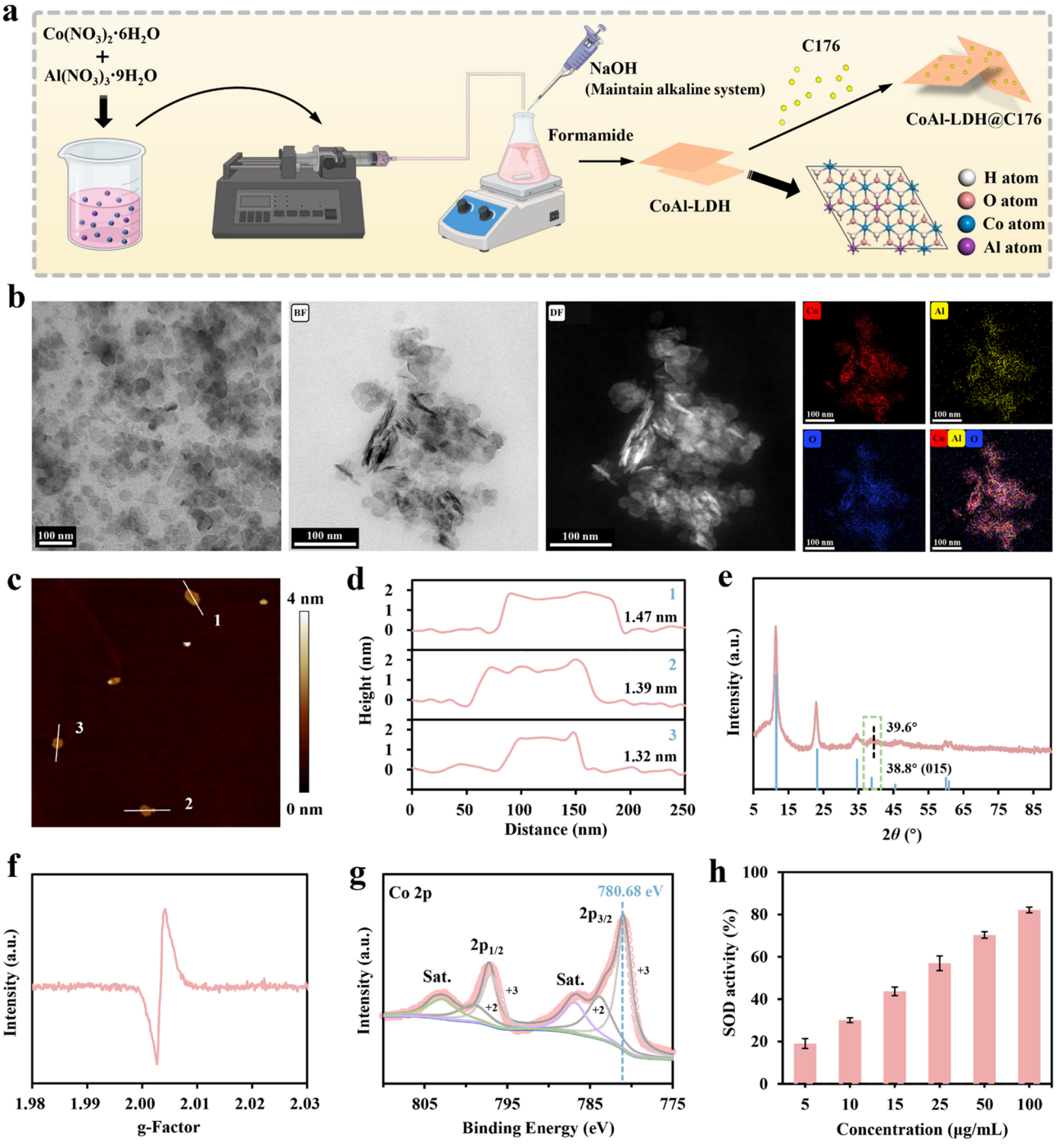

Fig. 1 Characterization of LDH and LDH/C. (**a**) The preparation schematic of LDH and LDH/C. (**b**) TEM image, bright-field image, dark-field image, and corresponding element mapping of LDH nanosheets. (**c**) AFM image, and (**d**) corresponding thickness of LDH. (**e**) XRD patterns and (**f**) EPR spectra of LDH nanosheets. (**g**) A high-resolution XPS spectrum of Co 2p in LDH nanosheets. (**h**) The SODase activity of LDH nanosheets with different concentration. The quantitative data in h reported as means ± S.D. from three independent replicates, and statistical significance was ascertained by a Student's *t*-test, with signifiers for *P*-values at $^{*}P < 0.05$, $^{**}P < 0.01$, and $^{***}P < 0.001$)

UV-Vis spectroscopic analysis confirmed the successful fabrication of LDH/C, as evidenced by distinct absorption features observed in the spectra of LDH, C176, and nanocomposite LDH/C (Figure S3). Moreover, the dynamic light scattering (DLS) analysis demonstrated that the mean diameter of LDH/C was found to be 59 nm (Figure S1). The binding of C176 to LDH occured via intermolecular forces, which subsequently enhance the solubility of C176. With increasing amounts of C176 added, the C176 loading efficiency of LDH exhibited a

gradual increase, reaching a maximum of 18.9% loading content at a drug addition concentration of 0.5 mg/mL (Figure S4-S5). Thus, LDH/C with 18.9% C176 was selected for further experiments. This standard of LDH/C was thus selected for subsequent experiments. The rapid release of the drug was achieved within the initial 12 h period, with a cumulative release of 29%. After then, a decrease in release rate was noted, with a continuous and gradual release of C176 from the LDH/C reached to 47% after 96 h (Figure S6). All the results demonstrated the successful preparation of LDH/C.

The binding capacity and colocalization analysis of DsDNA and LDH/C

The free dsDNA induces expression of inflammatory factors through the activation of the STING pathway, serving as a pivotal driver of inflammation. The accumulation of free dsDNA can lead to sustained overactivation of STING signaling, exacerbating pathological inflammation and contributing to the development of autoimmune responses. This highlights the critical importance of eliminating free DNA to maintain immune homeostasis and prevent pathological inflammation. To elucidate the molecular basis of LDH nanosheets on dsDNA, the interaction between LDH nanosheets and dsDNA fragments was investigated utilizing molecular dynamics (MD) simulations. The initial and final conformations of dsDNA binding to the surface of LDH nanosheets were demonstrated in Figure S7, and some snapshots were captured to illustrate the binding process (Fig. 2a, S8). To characterize the molecular bindings in the trajectories, the number of atomic contacts between dsDNA and LDH nanosheets was calculated quantitatively (Fig. 2b). In the initial stages, the dsDNA did not make contact with the surface of the LDH nanosheets. At approximately 19 nanoseconds, the number of contacts markedly increases to approximately 56, and the ends of the double-stranded DNA establish direct interactions with the LDH nanosheets. Subsequently, following a period of greater than 19 nanoseconds, the number of contacts remains relatively stable, indicating that the binding process is complete by forming stable bondings between dsDNA and LDH nanosheets.

To gain insight into the adsorbed molecular determinants and the interaction mechanisms of dsDNA to LDH nanosheets, the interaction energies including van der Waals (vdW) and Coulomb (Coul) energies have been calculated (Fig. 2c). It is noteworthy that the Coul and vdW energies decreased to -6.73 kJ/mol and -66.08 kJ/mol, respectively, at approximately $t = 19$ ns during the adsorption process. The pronounced decay of the vdW energy in comparison to the Coul energy indicates the preponderance of vdW interactions in dsDNA-LDH binding. Root mean square deviations (RMSDs) were further employed to evaluate the structural stability of dsDNA upon adsorption onto LDH nanosheets. The RMSD profiles exhibited mild fluctuations, indicating that the dsDNA retained its structural integrity throughout the MD trajectory (Fig. 2d). Atomic contact numbers and interaction energies exhibit slight fluctuations in the final stage of simulation, suggesting that the simulation is convergent. Furthermore, the minimum distance between base pairs and LDH nanosheets also reaches a stable value of 0.22 nm after $t > 19$ ns, providing additional evidence that the binding between dsDNA and LDH nanosheets exhibits high stability (Fig. 2e).

The interaction between dsDNA and LDH nanosheets was then investigated through agarose gel electrophoresis. Agarose gel electrophoresis showed that no dsDNA signals were discernible in the lanes of LDH-treated DNA, exhibiting minimal movement in comparison to naked DNA. This indicated a pronounced affinity between LDH nanosheets and DNA (Fig. 2f). While the movement of dsDNA was markedly slowed down as well, the binding ability of LDH/C to dsDNA was slightly weaker than that of LDH, as indicated by the presence of faint dsDNA signals in the corresponding lanes. Besides, when the dsDNA concentration was as high as 30 μg/mL, up to 90% of the dsDNA was adsorbed by LDH, indicating that LDH has an efficacious DNA adsorption capacity (Fig. 2g). Moreover, prolonging the incubation period of the different samples with DNA led to enhanced efficiency in DNA binding, reaching a plateau after approximately one hour (Fig. 2h).

The effects of LDH and LDH/C on the viability of Raw 264.7 cells were investigated by CCK8 and live/dead cell staining assays. The results demonstrated that the cells remained viable following LDH and LDH/C treatment, with no significant change in the proportion of live cells. This indicated that LDH and LDH/C were biocompatible and did not exhibit significant cytotoxic side effects (Figures S9-S10). In addition, the presence of LDH and LDH/C did not result in a decline in cell viability over time, and the proportion of live cells remained consistent (Figure S11), furhter verifying the low cytotoxic side effects. To further assess the ability of LDH/C to clear free DNA from cells, colocalization analysis of FITC-labelled nanosheets (FITC-LDH and FITC-LDH/C) and Cy5.5-labelled dsDNA was carried out. CpG 1826, a classic oligonucleotide, was utilized to simulate the released dsDNA from damaged cells. As shown in Fig. 2i, LDH and LDH/C could be effectively internalized into the cells, whereas both FITC-labelled nanosheets and Cy5.5-CpG have high colocalization rates, with Pearson coefficients value of 0.847 and 0.746, respectively. These findings indicated that both LDH and LDH/C possess remarkable intracellular dsDNA-binding abilities to effectively eliminate free DNA, thereby inhibiting the STING activation

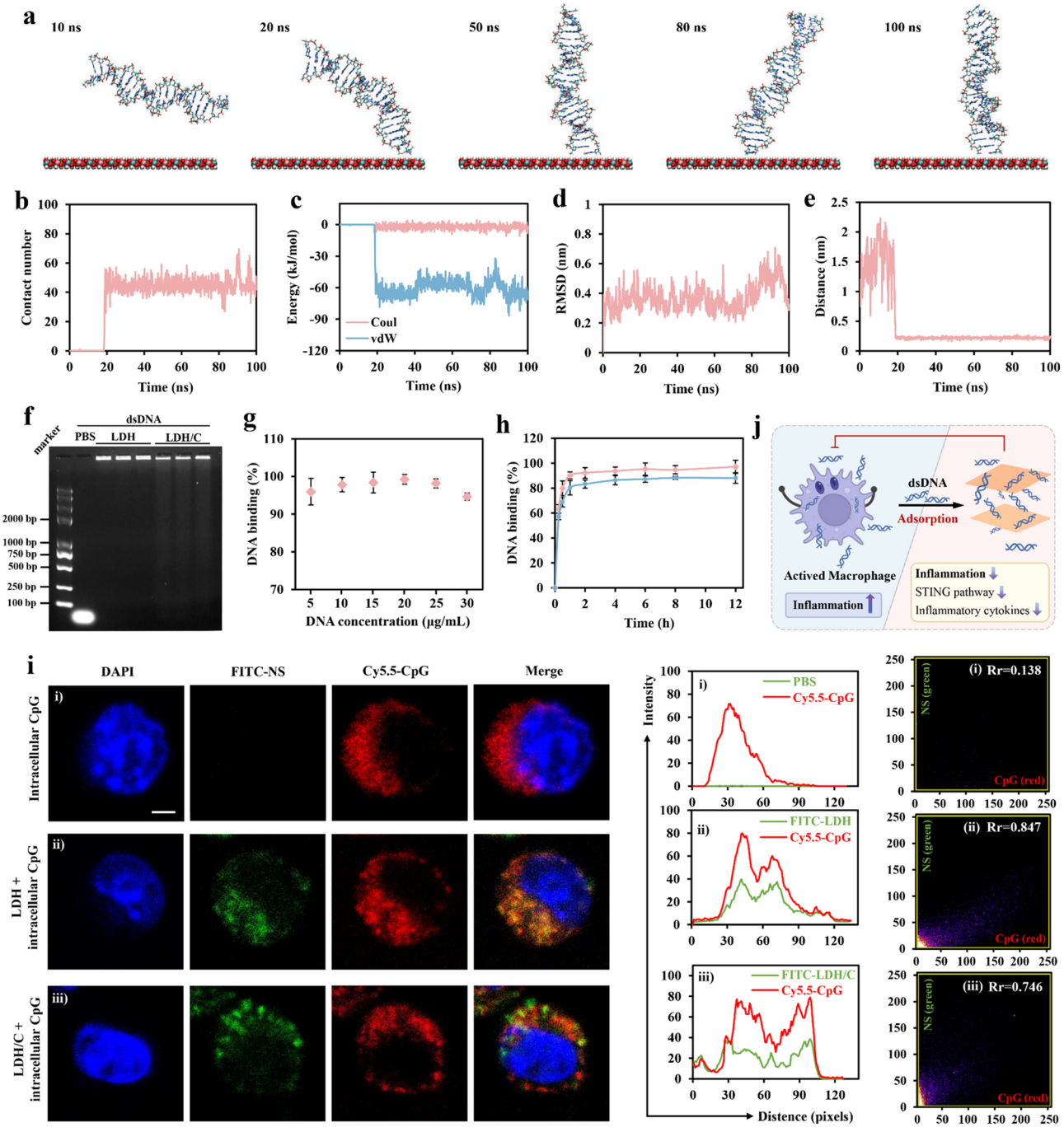

Fig. 2 LDH/C exhibits strong dsDNA-binding capabilities and effectively eliminates free dsDNA. (**a**) Representative snapshots for the binding process of dsDNA to LDH nanosheets at different key time points. (**b**) The time evolution of the contact number for the dsDNA adsorption process to the LDH nanosheets. (**c**) The van der Waals (vdW) and coulombic (Coul) energies between the dsDNA and the LDH nanosheets. (**d**) The root-mean-square deviation (RMSD) of dsDNA presented as a function of simulation time. (**e**) Time evolution of the minimum distance of the base pair from the LDH surface. (**f**) Agarose gel electrophoresis of free dsDNA, dsDNA + LDH, and dsDNA + LDH/C on 1.5% agarose gel. (**g**) The dsDNA binding percentages of LDH with various DNA concentration. (**h**) The dsDNA binding percentages of LDH or LDH/C as a function of incubation time. (**i**) Representative images, relative fluorescence intensity spectra, and Pearson's coefficient (Rr) of Raw 264.7 cells incubation with dsDNA (red), LDH (green), and DAPI staining (blue) for intracellular colocalization measured (scale bars: 2.5 μm). (**j**) The scheme of dsDNA absorption by LDH/C. The quantitative data in g and h reported as means ± S.D. from three independent replicates, and statistical significance was ascertained by a Student's *t*-test, with signifiers for *P*-values at $^{*}P < 0.05$, $^{**}P < 0.01$, and $^{***}P < 0.001$

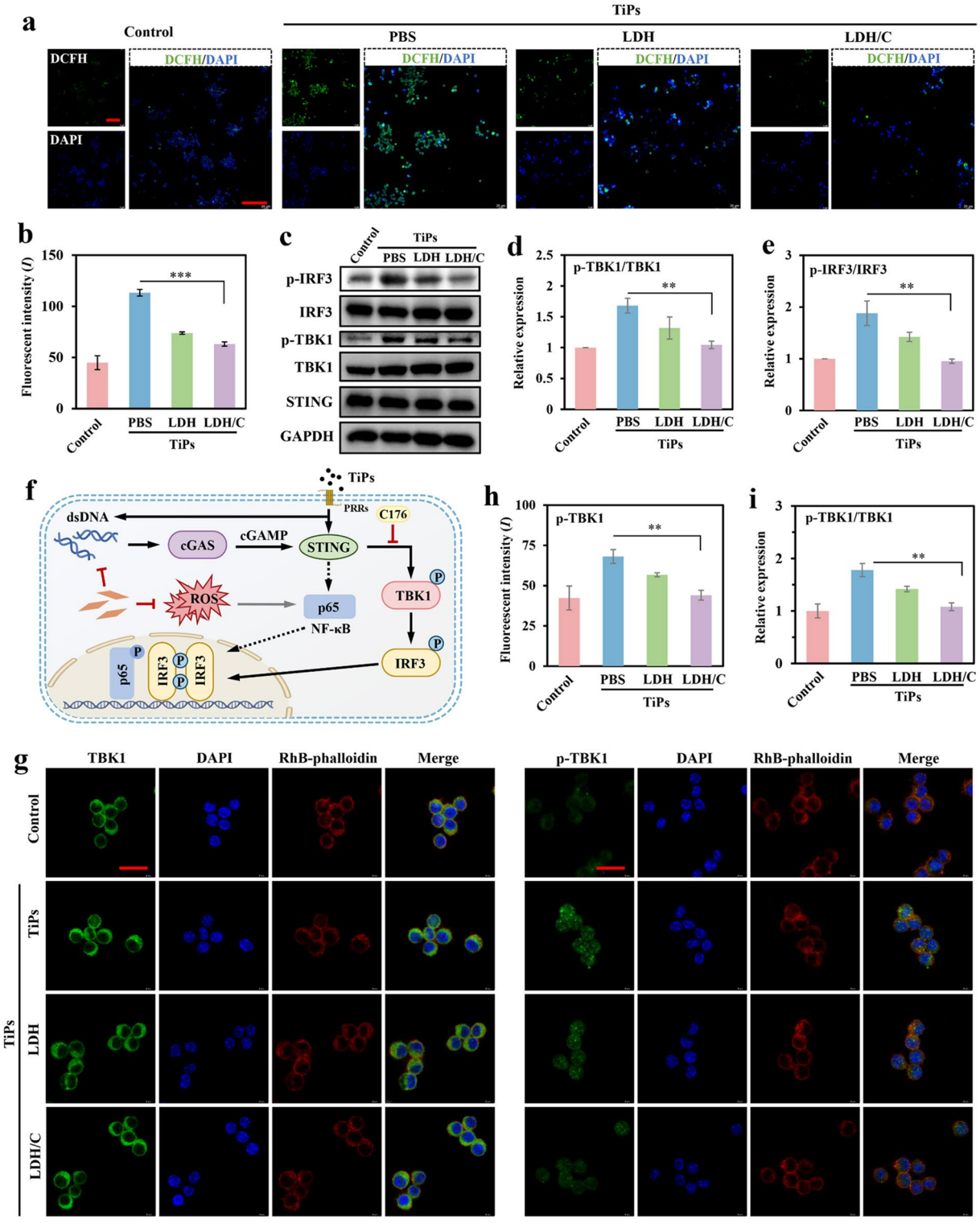

Fig. 3 (See legend on next page.)

caused by dsDNA. In a word, the results derived from MD simulations, agarose gel electrophoresis, and intracellular colocalization experiments collectively provide robust support for the hypothesis that LDH/C possesses the ability to bind DNA. By absorbing free DNA, LDH effectively inhibits the inflammatory response elicited by macrophage activation (Fig. 2j).

(See figure on previous page.)

Fig. 3 LDH/C inhibited over-activation of the STING pathway in vitro. (**a**) Representative images of Raw 264.7 cells for ROS detection with DCFH-DA (green) and DAPI staining (blue) after different treatments, scale bar: 100 μm. (**b**) Relative fluorescence intensity quantitative analysis of Raw 264.7 cells for ROS detection after different treatments. (**c**) Representative immunoblotting of p-IRF3, IRF3, p-TBK1, TBK1, and STING in BMDMs after indicated treatments, and GAPDH was employed as a control. (**d**-**e**) The relative protein expression quantitative analysis of (**d**) p-TBK1/TBK1, and (e) p-IRF3/IRF3. (f) Diagrammatic representation of the mechanism by which LDH/C inhibits the STING pathway. (**g**) Representative images of Raw 264.7 cells for TBK1 and p-TBK1 (green), RhB-phalloidin (red), and DAPI (blue) staining after different treatments (scale bar: 20 μm). (h-i) The relative fluorescence intensity quantitative analysis of (**h**) p-TBK1, and (**i**) p-TBK1/TBK1 in Raw 264.7 cells after various treatments. The quantitative data in b, d-e, and h-i reported as means ± S.D. from three independent replicates, and statistical significance was ascertained by a Student's *t*-test, with signifiers for *P*-values at $^{*}P < 0.05$, $^{**}P < 0.01$, and $^{***}P < 0.001$

LDH/C inhibited the elevation of intracellular ROS

Oxidative stress and inflammation are interdependent processes that concurrently occurred in an inflammatory milieu. In such contexts, elevated levels of ROS and oxidative stress byproducts can significantly augment the pro-inflammatory response. The clearance of ROS can assist in the reduction of oxidative stress, which in turn suppresses the pro-inflammatory response and contributes to the alleviation of inflammation. The prepared LDH nanosheets have been displayed to exhibit SODase-like activity, which can be attributed to the numerous vacancies on its surface, facilitating the scavenging of ROS and the alleviation of cellular damage caused by oxidative stress. The intracellular ROS scavenging ability of LDH was evaluated, and the cells were treated with TiPs, which were employed to simulate the effect of TiPs in contact with macrophages in vitro. The cellular immunofluorescence (IF) staining data revealed that both Raw 264.7 and bone marrow-derived macrophages (BMDMs) treated by TiPs exhibited a markedly elevated level of free radical fluorescence when compared to the cells of the control group. Concomitantly, the addition of LDH and LDH/C led to a substantial suppression of the fluorescence signal and the intracellular fluorescence intensity was markedly diminished, which is indicative of its scavenging capacity for free radicals (Figs. 3a-b, S12-S13).

LDH/C inhibited overactivation of the STING pathway in vitro

Based on the above findings regarding LDH/C's ability to bind dsDNA and scavenge elevated levels of ROS, the inhibitory effect of LDH/C on the STING pathway was further explored. The TiPs were selected as stimuli that activated the STING pathway through the TBK1/IRF3 axis, thereby triggering an inflammatory response. The effects of LDH/C on TiPs-induced STING activation in BMDMs were examined to investigate its therapeutic potential. The addition of LDH resulted in a significant reduction in the expression of p-TBK1 and p-IRF3, while LDH/C further decreased the expression of p-TBK1 and p-IRF3 to a level comparable to that observed in the untreated condition (Figs. 3c-e, S14). The potential mechanism by which LDH/C inhibiting the STING pathway was represented in Fig. 3f. As anticipated, the immunofluorescence images in Figs. 3g-i revealed a similar pattern to that in the immunoblotting data with a significant reduction of p-TBK1 expression observed in the presence of LDH and LDH/C. These results indicate that LDH/C exerted a more pronounced inhibitory effect on STING than other agents.

Activation of the NF-κB signaling pathway plays a pivotal role in macrophage inflammation. However, excessive stimulation can precipitate a severe inflammatory response and subsequent tissue damage, which may ultimately result in the onset of chronic inflammatory disorders. Inhibiting overactivation of the dysregulated pathway represents an imperative strategy for treating existing diseases. Well as expected, immunofluorescence staining demonstrated the co-localisation of p65 with the nucleus(Fig. 4a), indicating that p65, which was typically distributed in the cytoplasm, translocated into the nucleus in the presence of TiPs. This suggested the activation of NF-κB signalling pathway. Notably, p65 in LDH- or LDH/C-treated macrophages exhibited minimal translocation, retaining a predominantly cytoplasmic distribution. The results of the co-localisation analysis of p65 with the nucleus corroborated this observation (Fig. 4a, S15-S16). It can thus be concluded that LDH/C exerts an inhibitory effect on TiPs-induced macrophage inflammation.

LDH/C alleviated inflammation and inhibited osteoclasts resorption function

The preponderance of evidence underscores the critical role of peri-implant inflammation in the etiology of implant failure. Histological analyses of soft tissue biopsies from failed osteobiological implants reveal a marked inflammatory response associated with aggregates of titanium particles [46, 47]. The potential of LDH/C to inhibit TiPs-induced inflammatory responses was further investigated. The expression levels of the pro-inflammatory cytokines TNF-α and IL-6 were assessed by qPCR and ELISA. The results demonstrated that the presence of LDH and LDH/C resulted in a significant suppression of TiPs-induced overexpression of TNF-α (Fig. 4b and d). Concomitantly, IL-6 production was also found to be significantly reduced (Fig. 4c and e). The LDH/C group exhibited a particularly pronounced suppression of inflammation, as evidenced by a significant reduction in inflammatory cytokine secretion.

The infiltration of wear particles into the surrounding tissue will stimulate the overproduction of inflammatory cytokines, which will in turn lead to the polarization of macrophages into the M1 phenotype and the production of osteoclasts [48]. The impact of LDH on macrophage polarization was initially evaluated via flow cytometry. The findings indicated that macrophage polarization towards the M1 phenotype remained unaltered following treatment with varying concentrations of LDH (Figure S17-S18), suggesting that LDH does not markedly induce macrophage polarization towards the M1 phenotype within the concentration range tested. Following the induction of macrophages to polarize towards the M1 type by TiPs (100 mg/mL), these polarized macrophages were subsequently co-incubated with LDH or LDH/C. As shown in Fig. 4f, M1-type polarization of macrophages was markedly attenuated following co-incubation with LDH or LDH/C, suggesting that LDH and LDH/C possess the capacity to mitigate the M1-type polarization of macrophages.

Subsequently, the potential for inhibiting osteoclast activation was examined in the co-culture system of LDH/C and BMDMs. The osteoclast-specific TRAP staining demonstrated a striking reduction in both the number and area of osteoclasts and TRAP-positive cells in both the LDH and LDH/C groups (Fig. 4g and h and S19). Particularly, the LDH/C group exhibited a markedly more pronounced inhibition of osteoclast activation than the LDH group. The cytoskeletal staining further revealed that the number of both osteoclasts and F-actin rings were dramatically diminished and the podosome belt structure were impaired after treatment with LDH/C (Fig. 4i, S20). The release of TiPs from implants has been demonstrated to provoke a pronounced inflammatory response in macrophages as well as facilitating the osteoclastogenesis [49]. Our results indicate that LDH/C possesses the capacity to diminish the overall expression of both the inflammatory cytokines and osteoclastogenesis (Fig. 4j), thereby demonstrating its potential therapeutic role in the prevention of TiPs-induced osteolysis.

RNA-seq analysis of LDH/C

Following the identification of the role of LDH/C in scavenging ROS and anti-inflammatory thereby inhibiting osteoclastogenesis in vitro, an investigation was conducted to determine whether LDH/C might also have a protective role in the pathological setting of TiPs-induced osteolysis. To this end, high-throughput RNA sequencing (RNA-seq) was performed on differently treated Raw 264.7 cells in order to investigate the intrinsic molecular processes via which LDH/C affects osteoclastogenesis. The preliminary findings of the GO and KEGG analysis, which was conducted on the basis of whole genome sequencing of the cells, indicated that the overall status of the TiPs-treated cells was poor, which were severely damaged (Figure S21-S23). To further investigate the inflammatory inhibitory effect of LDH/C, whole genome sequencing analysis of LDH/C-treated cells was conducted. A total of 1,368 genes exhibited statistically significant differential gene expression, with 400 genes being up-regulated and 968 genes being down-regulated between the LDH/C and PBS groups under TiPs treatment (adjusted *P*-value cut-off <0.05). Of all the genes analyzed, Hmox-1 and Gclm exhibited the most pronounced upregulation (Fig. 5a-c). A heatmap was generated related nuclear factor erythroid 2-related factor 2 (Nrf2) and its downstream targets to illustrate the significant activation by LDH/C (Fig. 5d).

These changes were further explored by gene set-enrichment analysis, which confirmed the potent induction of the anti-inflammatory response by LDH/C. Indeed, the inflammatory pathways such as TNF signaling and NF-κB signaling were the most affected pathway in LDH/C-treated cells with a strong enrichment in antioxidant genes (Fig. 5e-f). As expected, KEGG pathway analysis of gene set-enrichment also confirmed the protective properties of treatments against osteolysis since innate immune pathways such as C-type lectin receptor signaling, Toll-like receptor signaling, and NOD-like receptor signaling, were ranked among the most down-regulated pathways upon LDH/C treatment (Fig. 5f). The enrichment of down-regulated genes in nucleic acid perception and immunity pathways such as Epstein-Barr virus infection and Hepatitis C points towards the involvement of activators of the innate immune cGAS-STING pathway, which could potentially explain the existence of free DNA and RNA. Indeed, the reduction of cfDNA may be achieved by the binding of LDH and cfDNA (Fig. 2j), which serves to inhibit innate immunity. These findings are in accordance with the existing literature on innate immune responses to TiPs [50].

LDH/C inhibited TiPs-induced mouse calvarial osteolysis in vivo

Encouraged by the effect of LDH/C on modulating STING activation and inflammation in vitro, the effects in a mice model of TiPs-induced inflammation osteolysis were further explored (Fig. 6a). Prior to the application of LDH/C in vivo, the systemic toxicity of LDH/C in mice was evaluated. No death and no significant changes in the bodyweights of the mice in each group were observed during the experimental period (Figure S24). Additionally, there were no discernible differences in the routine blood and blood biochemical parameters of the mice distributed across the various experimental groups (Figures S25-S26). Furthermore, the examination of liver and kidney tissue sections showed normal histology, indicating good biocompatibility of LDH/C (Figure S27).

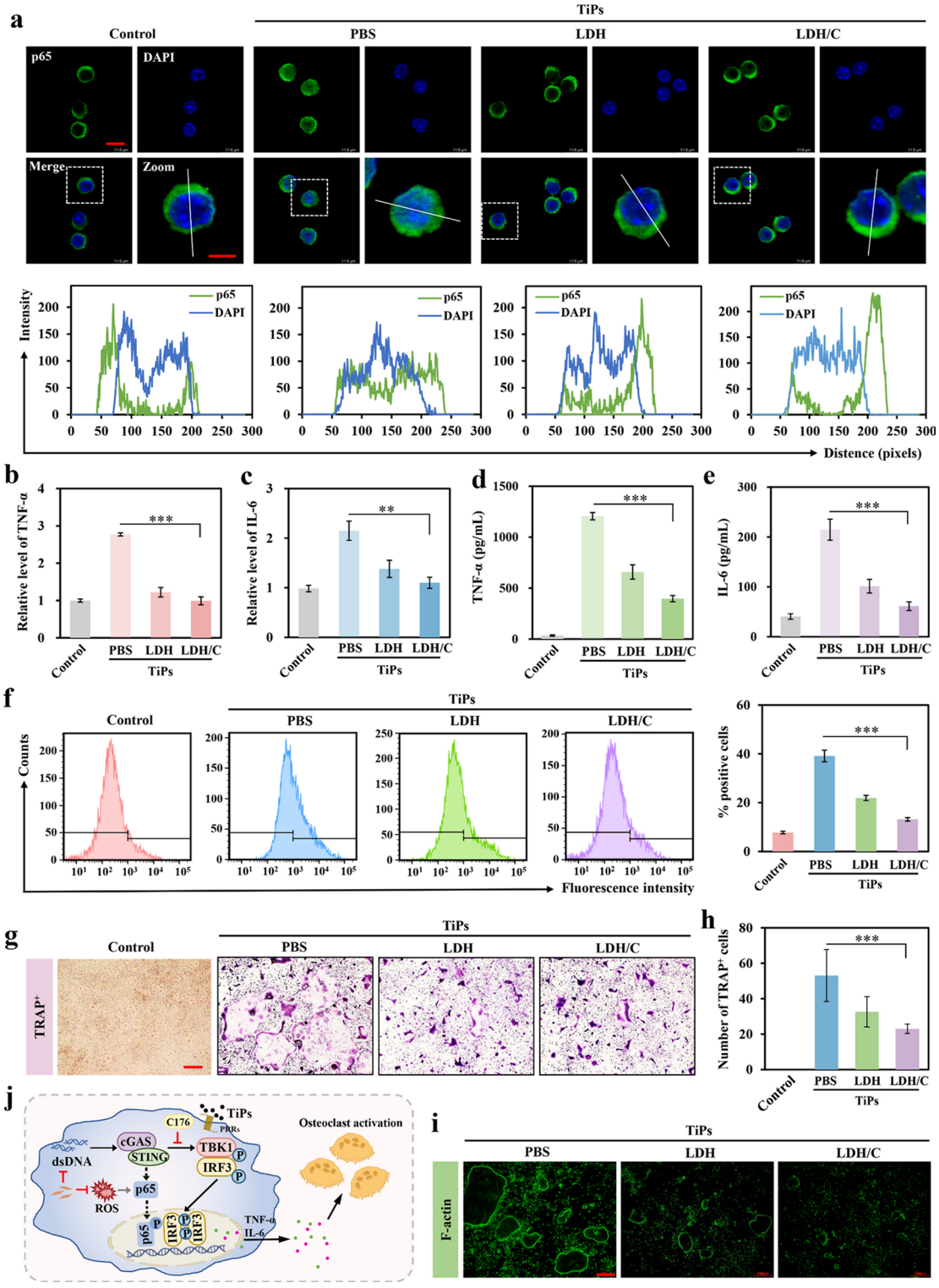

Fig. 4 LDH/C alleviates inflammation and inhibits osteoclast activation. (**a**) Representative images and intracellular colocalization fluorescence intensity spectra of Raw 264.7 cells incubation with p65 (green) and DAPI staining (blue) (scale bars: 10 μm and 5 μm). (**b**-**c**) The relative expressions level of (**b**) TNF-α and (c) IL-6 assessed by qPCR. ELISA of (**d**) TNF-α and (**e**) IL-6. (**f**) The M1 macrophages assessed by flow cytometry and the quantification of the positive rate of M1 macrophages with treatment of separate experimental groups. (**g**) Representative TRAP staining images of osteoclasts (scale bar = 500 μm). (**h**) Quantitation of number of TRAP-positive multinucleated cells with varying treatments. (**i**) Representative images for podosome belts with green fluorescent F-actin (scale bar = 500 μm). (**j**) A description of the mechanism of LDH/C-induced inhibition of osteoclast activation. The quantitative data in b-f and h reported as means ± S.D. from three independent replicates, and statistical significance was ascertained by a Student's *t*-test, with signifiers for *P*-values at $^{*}P < 0.05$, $^{**}P < 0.01$, and $^{***}P < 0.001$

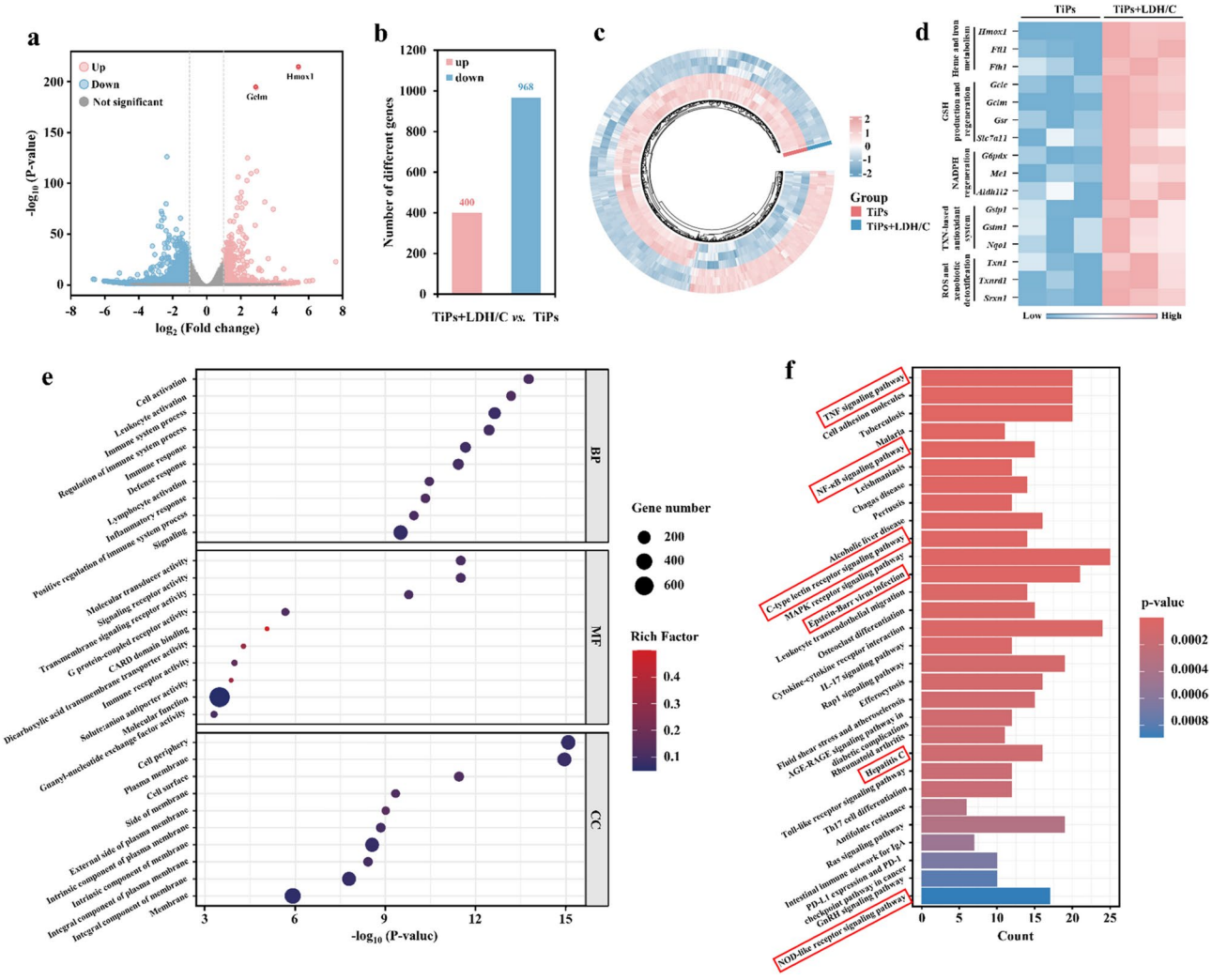

Fig. 5 Differentially expressed genes (DEG) and involved pathway of Raw 264.7 cells treated with TiPs followed by LDH/C treatment. (**a**) Volcano plot showing the distribution and expression changes of differential genes in the TiPs and TiPs + LDH/C groups. Genes highlighted in blue (indicating downregulated genes) and red (indicating upregulated genes) with absolute fold change > 2 and P value < 0.05, respectively. (**b**) The number of different genes after treated by TiPs and TiPs + LDH/C. (**c**) Heatmap of significantly differentially expressed genes from TiPs + LDH/C vs. TiPs (adjusted *P*-value cut-off < 0.05). (**d**) Heatmap of significantly differentially expressed genes with inflammation from TiPs + LDH/C vs. TiPs. (**e**, **f**) The (**e**) GO, and (**f**) KEGG enrichment of downregulated DEG in the TiPs and TiPs + LDH/C groups

As demonstrated by the 3D reconstructed images and transverse sections of mouse crania in Fig. 6b, the TiPs experimental group, which served as the osteolysis model, exhibited severe erosion of the cranium, accompanied by notable thinning of the bone and destruction of cranial sutures. These observations confirmed the successful construction of the osteolysis model. A comparison of the TiPs group with the other three experimental groups revealed a significantly reduced area of osteolysis in the mouse cranium, indicative of an alleviating effect of LDH, C176, and LDH/C on the destruction of bone erosion. Of note, the lowest degree of osteolysis was observed in the cranial bones of mice in the LDH/C group, thereby demonstrating the most evident inhibitory effect of LDH/C on TiPs-induced inflammatory osteolysis. The statistical analysis of bone-related parameters revealed that the bone mineral density, bone volume fraction, and trabecular number of the cranium of mice in the TiPs experimental group were significantly reduced in comparison to the sham-operated group, while trabecular separation was significantly increased. In contrast, the administration of LDH/C treatment was found to reverse the TiPs-induced changes in bone parameters, which significantly suppressed the severity of TiPs-induced osteolysis (Fig. 6c and f).

The results of the micro-CT analysis were corroborated by the findings of the H&E staining, which demonstrated that LDH/C significantly alleviated the severity of cranial bone destruction induced by TiPs. Additionally, the inflammatory response was markedly reduced,

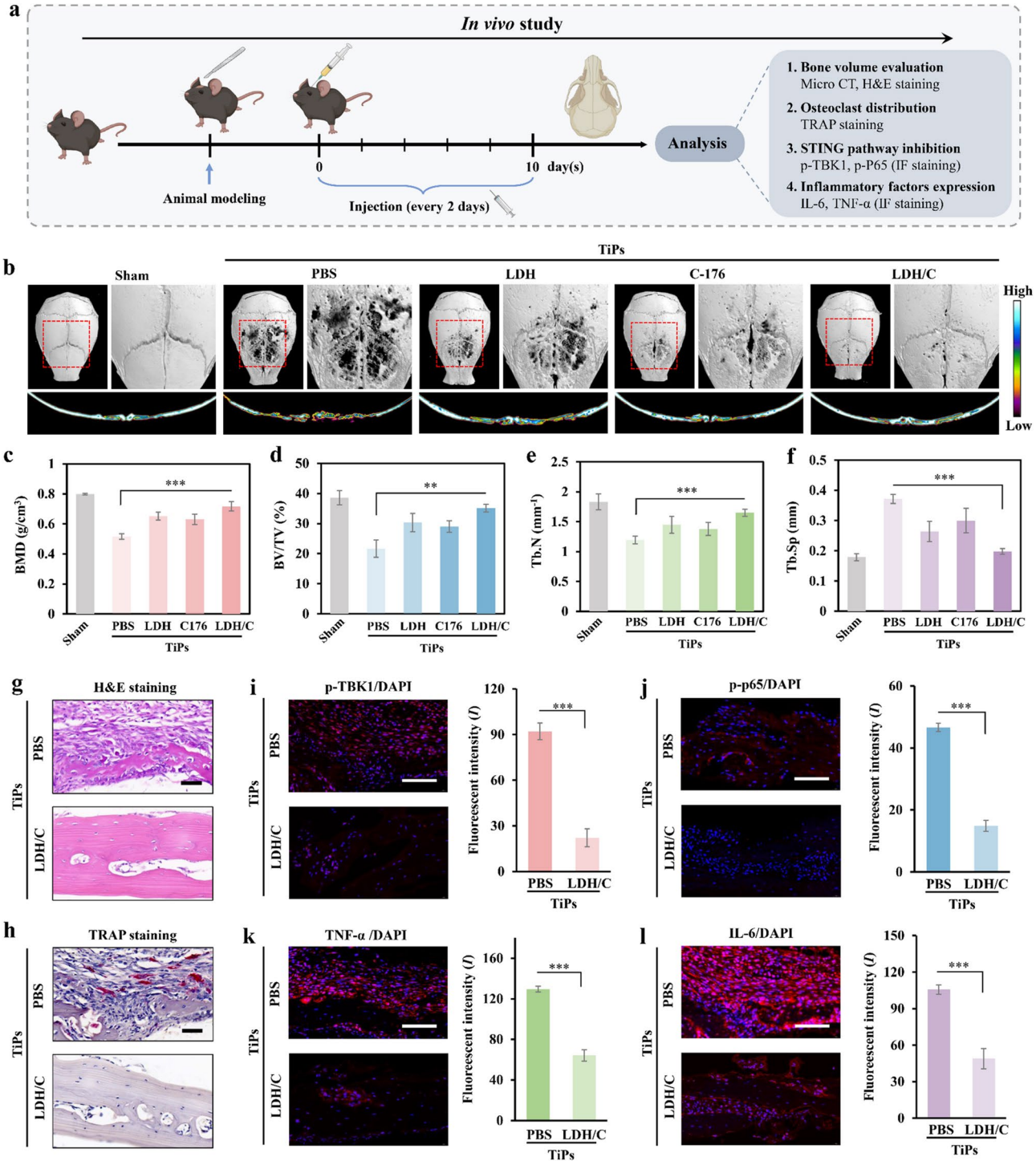

Fig. 6 LDH/C mitigates the pathological manifestations associated with TiPs-induced mice inflammation osteolysis. (**a**) The experimental timeline for conducting the mice inflammation osteolysis experiment in vivo. (**b**) Micro-CT scanner reconstructions and transverse sections (pseudocolor) of the calvarial anatomy from each experimental cohort. Quantitatively analyzed parameters of (**c**) bone mineral density (BMD), (**d**) bone volume percentage (BV/TV), (**e**) trabecular number (Tb.N.), and (**f**) trabecular separation (Tb.Sp). (**g**) Calvaria sections from each mouse group subjected to H&E staining (scale bar = 50 μm). (**h**) Calvaria sections from each mouse group subjected to TRAP staining (scale bar = 50 μm). Immunohistochemical assays and quantitative analysis for (**i**) p-TBK1, (**j**) p-p65, (**k**) TNF-α, and (**l**) IL-6 (all marked in red while DAPI marked in blue) (scale bars at 200 μm and zoomed in at 100 μm for detailed images). The quantitative data in c-f and i-l reported as means ± S.D. from five independent replicates, and statistical significance was ascertained by a Student's *t*-test, with signifiers for *P*-values at $^{*}P < 0.05$, $^{**}P < 0.01$, and $^{***}P < 0.001$

accompanied by a notable decline in the number of inflammatory cells (Fig. 6g and S28). The TRAP staining further revealed that LDH/C treatment resulted in a reduction in the number of TRAP-positive osteoclasts, thereby attenuating bone erosion by inhibiting osteoclast differentiation and formation (Fig. 6h and S29). Furthermore, immunofluorescence staining demonstrated that the activation of the STING pathway was inhibited by LDH/C treatment, with a notable reduction in the expression of p-TBK1 (Fig. 6i and S30-S31). Similarly, the expression level of p-p65 demonstrated a consistent and statistically significant downward trend (Fig. 6j and S32-S33). IF stain analysis revealed that tissues from LDH/C-treated mice exhibited a significant reduction in M1 markers ($CD86^+$) alongside increased M2 markers ($CD206^+$) compared to TiPs group (S34-S35). As anticipated, the immune-fluorescence staining results for TNF-α and IL-6 were in accordance with the in vitro expression levels, and LDH/C demonstrated its capability to attenuate the inflammatory response caused by TiPs (Fig. 6k and l, and S36-S39). In a word, LDH/C was found to efficiently suppress the level of oxidative stress and STING signaling at the site of inflammation, attenuating the pathological changes associated with TiPs-induced inflammatory osteolysis in vivo.

Conclusion

Herein, a synergistic approach was proposed to manage aseptic inflammation surrounding the periprosthesis, aiming to normalize local bone metabolism and thereby mitigate wear-particle-induced periprosthetic osteolysis. The synthesized LDH/C showed antioxidant nano-enzymatic activity, effectively modulating oxidative stress levels within the local microenvironment. Such SODase-like activity improved the inflammatory microenvironment, thereby remodeling the bone homeostasis. Additionally, LDH/C was found to simultaneously adsorb dsDNA and inhibit STING activation. The effective binding of cfNDA on LDH was primarily facilitated by van der Waals energy, which in turn interfered with cfDNA-associated pro-inflammatory signaling and intercellular communication. Combined with C176 that selectively block and suppress hyperactivation of the cGAS-STING signaling cascade, the proposed strategy synergistically inhibited the STING pathway and reduced oxidative stress levels, contributing to the alleviation of osteolysis-related inflammation and pathology. Our study offers new avenues for clinical intervention in periprosthetic osteolysis, as well as new perspectives into regulatory strategies for key inflammatory mediators and the disruption of pro-inflammatory signaling.

Supplementary Information

The online version contains supplementary material available at https://doi.org/10.1186/s12951-025-03458-z.

Supplementary Material 1

Acknowledgements

This work was supported by the National Natural Science Foundation of China (82372098).

Author contributions

Z. F.: Conceptualization, Investigation, Data curation, Formal analysis, Methodology, Validation, Writing - original draft. M. Z.: Conceptualization, Data curation, Validation, Visualization, Writing - review & editing. Y. H.: Data curation, Methodology, Supervision, Validation. H. W., W. H.: Formal analysis, Supervision, Validation. Z. L.: Validation, Writing - review & editing. H. G.: Conceptualization, Supervision, Writing - review & editing. D. N.: Conceptualization, Funding acquisition, Investigation, Supervision, Writing - review & editing. All authors discussed the data and reviewed the manuscript.

Data availability

No datasets were generated or analysed during the current study.

Declarations

Ethics and consent to publish

All animal experiments were authorized by the Ethics Committee of the Shanghai Jiao Tong University (A2023128-001).

Competing interests

The authors declare no competing interests.

Received: 1 April 2025 / Accepted: 9 May 2025
Published online: 27 May 2025

References

1. Ormsby RT, Solomon LB, Yang D, Crotti TN, Haynes DR, Findlay DM, Atkins GJ. Osteocytes respond to particles of clinically-relevant conventional and cross-linked polyethylene and metal alloys by up-regulation of resorptive and inflammatory pathways. Acta Biomater. 2019;87:296–306.
2. Wu Y, He F, Zhang C, Zhang Q, Su X, Zhu X, Liu A, Shi W, Lin W, Jin Z, Yang H, Lin J. Melatonin alleviates titanium nanoparticles induced osteolysis via activation of butyrate/GPR109A signaling pathway. J Nanobiotechnol. 2021;19(1):170.
3. Springer BD, Sotile WM. The psychology of total joint arthroplasty. J GROMACS Arthroplasty. 2020;35(6S):S46–9.
4. Tian Y, Terkawi MA, Onodera T, Alhasan H, Matsumae G, Takahashi D, Hamasaki M, Ebata T, Aly MK, Kida H, Shimizu T, Uetsuki K, Kadoya K, Iwasaki N. Blockade of XCL1/Lymphotactin ameliorates severity of periprosthetic osteolysis triggered by Polyethylene-Particles. Front Immunol. 2020;11:1720.
5. Fritz EA, Glant TT, Vermes C, Jacobs JJ, Roebuck KA. Chemokine gene activation in human bone marrow-derived osteoblasts following exposure to particulate wear debris. J Biomed Mater Res A. 2006;77(1):192–201.
6. Ollivere B, Wimhurst JA, Clark IM, Donell ST. Current concepts in osteolysis. J Bone Joint Surg Br. 2012;94(1):10–5.
7. Ormsby RT, Cantley M, Kogawa M, Solomon LB, Haynes DR, Findlay DM, Atkins GJ. Evidence that osteocyte perilacunar remodelling contributes to polyethylene wear particle induced osteolysis. Acta Biomater. 2016;33:242–51.
8. Cao J, Ma X, Liu L, Zhang G, Wu Y, Fu Y, Gong A, Yang Z, Zhao Y, Zhang L, Li Y. Cortistatin attenuates titanium particle–induced osteolysis through regulation of TNFR1–ROS–caspase-3 signaling in osteoblasts. Ann N Y Acad Sci. 2022;1513(1):140–52.
9. Yang H, Xu Y, Zhu M, Gu Y, Zhang W, Shao H, Wang Y, Ping Z, Hu X, Wang L, Geng DJB. Inhibition of titanium-particle-induced inflammatory osteolysis after local administration of dopamine and suppression of osteoclastogenesis via D2-like receptor signaling pathway. Biomaterials. 2016;80:1–10.

10. Wang H, Hsu JC, Song W, Lan X, Cai W, Ni D. Nanorepair medicine for treatment of organ injury. Natl Sci Rev. 2024;11(9):nwae280.
11. Tu Z, Zhong Y, Hu H, Shao D, Haag R, Schirner M, Lee J, Sullenger B, Leong KW. Design of therapeutic biomaterials to control inflammation. Nat Rev Mater. 2022;7(7):557–74.
12. Galluzzi L, López-Soto A, Kumar S, Kroemer G. Caspases connect Cell-Death signaling to organismal homeostasis. Immunity. 2016;44(2):221–31.
13. Yang H, Wang H, Ren J, Chen Q, Chen ZJ. cGAS is essential for cellular senescence. Proc Natl Acad Sci U S A. 2017;114(23):E4612–20.
14. Glück S, Guey B, Gulen MF, Wolter K, Kang T-W, Schmacke NA, Bridgeman A, Rehwinkel J, Zender L, Ablasser A. Innate immune sensing of cytosolic chromatin fragments through cGAS promotes senescence. Nat Cell Biol. 2017;19(9):1061–70.
15. Burdette DL, Vance RE. STING and the innate immune response to nucleic acids in the cytosol. Nat Immunol. 2013;14(1):19–26.
16. Motwani M, Pawaria S, Bernier J, Moses S, Henry K, Fang T, Burkly L, Marshak-Rothstein A, Fitzgerald KA. Hierarchy of clinical manifestations in SAVI N153S and V154M mouse models. Proc Natl Acad Sci U S A. 2019;116(16):7941–50.
17. Ablasser A, Chen ZJ. cGAS in action: expanding roles in immunity and inflammation. Science. 2019;363(6431):eaat8657.
18. Taguchi T, Mukai K. Innate immunity signalling and membrane trafficking. Curr Opin Cell Biol. 2019;59:1–7.
19. Haag SM, Gulen MF, Reymond L, Gibelin A, Abrami L, Decout A, Heymann M, van der Goot FG, Turcatti G, Behrendt R, Ablasser A. Targeting STING with covalent small-molecule inhibitors. Nature. 2018;559(7713):269–73.
20. Pham PT, Fukuda D, Nishimoto S, Kim-Kaneyama J-R, Lei X-F, Takahashi Y, Sato T, Tanaka K, Suto K, Kawabata Y, Yamaguchi K, Yagi S, Kusunose K, Yamada H, Soeki T, Wakatsuki T, Shimada K, Kanematsu Y, Takagi Y, Shimabukuro M, Setou M, Barber GN, Sata M. STING, a cytosolic DNA sensor, plays a critical role in atherogenesis: a link between innate immunity and chronic inflammation caused by lifestyle-related diseases. Eur Heart J. 2021;42(42):4336–48.
21. Wu B, Xu M, Fan C, Feng C, Lu Q, Lu H, Xiang C, Bai F, Wang H, Wu Y, Tang W. STING inhibitor ameliorates LPS-induced ALI by preventing vascular endothelial cells-mediated immune cells chemotaxis and adhesion. Acta Pharmacol Sin. 2021;43(8):2055–66.
22. Shen H, Jin L, Zheng Q, Ye Z, Cheng L, Wu Y, Wu H, Jon TG, Liu W, Pan Z, Mao Z, Wang Y. Synergistically targeting synovium STING pathway for rheumatoid arthritis treatment. Bioact Mater. 2023;24:37–53.
23. Han B, Wang X, Wu P, Jiang H, Yang Q, Li S, Li J, Zhang Z. Pulmonary inflammatory and fibrogenic response induced by graphitized multi-walled carbon nanotube involved in cGAS-STING signaling pathway. J Hazard Mater. 2021;417:125984.
24. Peng Y, He D, Ge X, Lu Y, Chai Y, Zhang Y, Mao Z, Luo G, Deng J, Zhang Y. Construction of heparin-based hydrogel incorporated with Cu5.4O ultrasmall nanozymes for wound healing and inflammation Inhibition. Bioact Mater. 2021;6(10):3109–24.
25. Lohmann N, Schirmer L, Atallah P, Wandel E, Ferrer RA, Werner C, Simon JC, Franz S, Freudenberg U. Glycosaminoglycan-based hydrogels capture inflammatory chemokines and rescue defective wound healing in mice. Sci Transl Med. 2017;9(386):eaai9044.
26. Ying F, Chalise JP, Narendra SC, Magnusson M. Type I IFN protects against antigen-induced arthritis. Eur J Immunol. 2011;41(6):1687–95.
27. Liu Y, Jesus AA, Marrero B, Yang D, Ramsey SE, Montealegre Sanchez GA, Tenbrock K, Wittkowski H, Jones OY, Kuehn HS, Lee C-CR, DiMattia MA, Cowen EW, Gonzalez B, Palmer I, DiGiovanna JJ, Biancotto A, Kim H, Tsai WL, Trier AM, Huang Y, Stone DL, Hill S, Kim HJ, Gurprasad C, Plass N, Chapelle D, Horkayne-Szakaly I, Foell D, Barysenka A, Candotti F, Holland SM, Hughes JD, Mehmet H, Issekutz AC, Raffeld M, McElwee J, Fontana JR, Minniti CP, Moir S, Kastner DL, Gadina M, Steven AC, Wingfield PT, Brooks SR, Rosenzweig SD, Fleisher TA, Deng Z, Boehm M, Paller AS, Goldbach-Mansky R. Activated STING in a Vascular and Pulmonary Syndrome, New Engl J Med. 2014;371(6):507–518.
28. Peng B, Liang H, Li Y, Dong C, Shen J, Mao HQ, Leong KW, Chen Y, Liu L. Tuned cationic dendronized polymer: molecular scavenger for rheumatoid arthritis treatment. Angew Chem Int Ed Engl. 2019;58(13):4254–8.
29. Liang H, Peng B, Dong C, Liu L, Mao J, Wei S, Wang X, Xu H, Shen J, Mao H, Gao X, Leong KW, Chen Y. Cationic nanoparticle as an inhibitor of cell-free DNA-induced inflammation. Nat Commun. 2018;9(1):4291.
30. Hu T, Gu Z, Williams GR, Strimaite M, Zha J, Zhou Z, Zhang X, Tan C, Liang R. Layered double hydroxide-based nanomaterials for biomedical applications. Chem Soc Rev. 2022;51(14):6126–76.
31. Li L, Soyhan I, Warszawik E, van Rijn P. Layered double hydroxides: recent progress and promising perspectives toward biomedical applications. Adv Sci. 2024;11(20):e2306035.
32. Kankala RK. Nanoarchitectured two-dimensional layered double hydroxides-based nanocomposites for biomedical applications. Adv Drug Deliv Rev. 2022;186:114270.
33. Tejero J, Shiva S, Gladwin MT. Sources of vascular nitric oxide and reactive oxygen species and their regulation. Physiol Rev. 2019;99(1):311–79.
34. Sies H, Belousov VV, Chandel NS, Davies MJ, Jones DP, Mann GE, Murphy MP, Yamamoto M, Winterbourn C. Defining roles of specific reactive oxygen species (ROS) in cell biology and physiology. Nat Rev Mol Cell Biol. 2022;23(7):499–515.
35. Wang L, Zhu B, Deng Y, Li T, Tian Q, Yuan Z, Ma L, Cheng C, Guo Q, Qiu L. Biocatalytic and Antioxidant Nanostructures for ROS Scavenging and Biotherapeutics, Adv Funct Mater. 2021;31:2101804.
36. Zhao Y, Zhang X, Jia X, Waterhouse GIN, Shi R, Zhang X, Zhan F, Tao Y, Wu L-Z, Tung C-H, O'Hare D, Zhang T. Sub-3 Nm ultrafine monolayer layered double hydroxide nanosheets for electrochemical water oxidation. Adv Energy Mater. 2018;8(18):1703585.
37. Li H, Shi J, Zhao K, Zhang L. Sustainable molecular oxygen activation with oxygen vacancies on the {001} facets of BiOCl nanosheets under solar light. Nanoscale. 2014;6(23):14168–73.
38. Zhang S, Chen J, Yang W, Chen X. Vacancies-rich coal monolayer layered double hydroxide as efficient superoxide dismutase-like nanozyme. Nano Res. 2022;15(9):7940–50.
39. Dong J, Song L, Yin J-J, He W, Wu Y, Gu N, Zhang Y. Co_3O_4 nanoparticles with Multi-Enzyme activities and their application in immunohistochemical assay. ACS Appl Mater Interfaces. 2014;6(3):1959–70.
40. Zhao Y, Chen G, Bian T, Zhou C, Waterhouse GI, Wu LZ, Tung C, Smith LJ, O'Hare D, Zhang T. Defect-Rich ultrathin ZnAl-Layered double hydroxide nanosheets for efficient photoreduction of CO_2 to CO with water. Adv Mater. 2015;27(47):7824–31.
41. Vernekar AA, Das T, Mugesh G. Vacancy-Engineered nanoceria: enzyme mimetic hotspots for the degradation of nerve agents. Angew Chem Int Ed Engl. 2016;55(4):1412–6.
42. Li X. Improved pyrogallol autoxidation method: A reliable and cheap Superoxide-Scavenging assay suitable for all antioxidants. J Agric Food Chem. 2012;60(25):6418–24.
43. Wu G, Berka V, Derry PJ, Mendoza K, Kakadiaris E, Roy T, Kent TA, Tour JM, Tsai A. Critical comparison of the superoxide Dismutase-like activity of carbon antioxidant nanozymes by direct superoxide consumption kinetic measurements. ACS Nano. 2019;13(10):11203–13.
44. Jiang B, Duan D, Gao L, Zhou M, Fan K, Tang Y, Xi J, Bi Y, Tong Z, Gao GF, Xie N, Tang A, Nie G, Liang M, Yan X. Standardized assays for determining the catalytic activity and kinetics of peroxidase-like nanozymes. Nat Protoc. 2018;13(7):1506–20.
45. Korschelt K, Ragg R, Metzger CS, Kluenker M, Oster M, Barton B, Panthöfer M, Strand D, Kolb U, Mondeshki M, Strand S, Brieger J, Nawaz Tahir M, Tremel W. Glycine-functionalized copper(ii) hydroxide nanoparticles with high intrinsic superoxide dismutase activity. Nanoscale. 2017;9(11):3952–60.
46. Scales JT. Black staining around titanium alloy prostheses–an orthopaedic enigma. J Bone Joint Surg Br. 1991;73(4):534–6.
47. Witt JD, Swann M. Metal wear and tissue response in failed titanium alloy total hip replacements. J Bone Joint Surg Br. 1991;73(4):559–63.
48. Yan Z, Tian X, Zhu J, Lu Z, Yu L, Zhang D, Liu Y, Yang C, Zhu Q, Cao X. Metformin suppresses UHMWPE particle-induced osteolysis in the mouse calvaria by promoting polarization of macrophages to an anti-inflammatory phenotype. Mol Med. 2018;24(1):20.
49. Eger M, Sterer N, Liron T, Kohavi D, Gabet Y. Scaling of titanium implants entrains inflammation-induced osteolysis. Sci Rep. 2017;7:39612.
50. Ouyang Z, Xu J, Liu T, Lin S, Sun Y, Huang Y, Zheng Z, Zeng G, Li C, Li S, Ding Y. STING/TBK1 regulates inflammation in macrophages and titanium Particles-Induced osteolysis. ACS Biomater Sci Eng. 2023;9(6):3273–84.

Publisher's note